Time-Resolved Photoluminescence Studies of InGaP Nanowires for Improving the Internal Quantum Efficiency

Master's Thesis

Author:
Lert Chayanun

Supervisor:
Asst. Prof. Niklas Sköld

LUND
UNIVERSITY

Project duration: 3months

Spring 2016

Division of Solid State Physics
Department of Physics, Faculty of Science
Lund University

Abstract

Semiconductor Nanowires are promising building blocks for advanced optoelectronic devices since their small diameter give rise to quantization effects. The small diameter also makes them susceptible to non-radiative recombination due to surface states. A consequence of non-radiative surface recombination is a reduction of a total recombination lifetime. This is in turn limits an internal quantum efficiency (IQE) of optoelectronic devices because the IQE is defined as a ratio between the radiative recombination lifetime and the total recombination lifetime. It is therefore important to produce the nanowires with as long total lifetime as possible in order to achieve a significant IQE.

This thesis aims to improve the IQE of the nanowires by using the surface passivating layer with a larger bandgap material on ternary alloy (InGaP) nanowires. The larger bandgap of the passivating layer will allocate the charge carriers into the center nanowire which, therefore, decrease the chance of the recombination at the surface. The passivating layer covers the side facet of the nanowires as a shell. The nanowires with this shell layer are called core-shell nanowires.

Photoluminescence (PL) spectroscopy was used to evaluate the material composition and the bandgap of the core nanowire as well as the shell layer. Various compositions of shell materials give different band offsets between the core and the shell. Time-resolved photoluminescence (TRPL) was performed on the nanowires with and without the shell to measure the recombination lifetime. Finally, the energy structure of the non-radiative recombination center was studied by a temperature dependent PL (TDPL) and a power dependent TRPL.

For the plain nanowires, the result shows that the non-radiative recombination is indeed related to surface states as expected. The total lifetime of the thinner wires is shorter than the thicker wires. Therefore, the IQE will degrade for the devices based on the thin nanowires. The TDPL reveals that the intensity is two orders of magnitude lower at room temperature (300 K) compared with the lowest measured temperature (4 K). The decreasing intensity is a result of two quenching processes. As the temperature increases, charge carriers gain higher thermal energies. The first quenching process occurs as the charge carriers escape the potential confinement with their higher thermal energies. Another process corresponds to a non-radiative recombination center with an activation energy of 17 meV. Power dependent TRPL at low (5 K) and high (100 K) temperature confirmed that the non-radiative recombination center is thermally activated.

Popular description

The performance of the computer processor has improved drastically over the past decade through an increasing number of transistors employed on a single processor chip. A simple approach for having a larger amount of transistors on a single circuit is to scale down the device. The smallest feature of a transistor is for example only a few nanometers (nm=0.000000001m) large which is about ten thousand times smaller than human's hair. However, electrical and optical properties of miniaturized devices are impacted by quantum effects, such as energy quantization, and tunneling. These effects can either limit or improve the performance of the devices.

A new nanostructure, *Semiconductor Nanowire*, is introduced as a building block of advanced electrical devices. It is a semiconductor material with a cylindrical shape, in which the diameter can be on a scale of nanometers and the length is about a few micrometers. The configuration of the nanowire provides a large surface comparing to its volume. With its large surface, it is therefore suitable for sensing applications, especially as an optoelectronic device. The purpose of the optoelectronic devices is to be either a light detector or a light source. For the nanowire as the light detector, the absorbed light excites electrons from a stationary state to move freely within the nanowire. Those free electrons make the device electrically conductive. For the light source, the electrons can be excited by an external energy; such as electricity or light. The excited electrons would then relax back to their stationary state whereupon release the excess energy in the form of light.

The efficiency of those devices is determined by how well the energy is transferred between the free electrons and the light. An ideal condition is that every electron should emit the light as it relaxes for the light source. In contrast for the light detector, all the absorbed light should give rise to the free electrons. However, defects in the material and the surfaces of the devices can create "dark" pathways for the electrons to relax without the light emission. This makes the device less efficient. This is problematic since the nanowires are so thin that electrons are always close to the surface. There is a method called surface passivation which most surface of the wire is covered by another semiconductor material. With the proper passivation, the free electrons will move away from the surface. Consequently, the "dark" pathways can be avoided.

In this study, there are several measurements performed on the nanowires with and without surface passivation in order to compare the device performance. The performance of the nanowires is expected to be improved when employing the surface passivation. Also, the study is to better understand the "dark" pathways involving the surface condition of the nanowires.

Preface

This report contains my thesis work which includes PL, TDPL, and TRPL measurement performed on the nanowire samples to evaluate the total recombination lifetime of the device. That information leads to an interpretation of the IQE of the nanowires. The principles of carrier's recombination mechanisms and lifetime are described in Chapter 1. Then, Chapter 2 explains the methods of each measurement while the results of the measurement are discussed in Chapter 3. The details of the nanowire growth process are mentioned in Chapter 1 and Chapter 2. Finally, the outcome of this work is enclosed in Chapter 4.

I would like to thank my supervisor, Asst. Prof. Niklas Sköld, who constantly helps to provide the equipment and to set up everything for the measurement. Besides, with his strong knowledge of optoelectronics and semiconductor physics, he can always give good advice on the result interpretation. Also, he usually gives a useful guidance to conduct the research.

Last but not least, thank you to my parents and my sisters for your support.

Lert Chayanun
May 2016

List of abbreviations

AOM	Acousto-optic modulator
APD	Avalanche photodiode
BS	Beam splitters
CCD	Charge-coupled device
CW	Continuous wave
eeh	Electron-electron-hole
ehh	Electron-hole-hole
FWHM	Full-width-half-maximum
IQE	Internal quantum efficiency
LD	Laser diode
LED	Light emitting diode
MOVPE	Metal-organic vapor phase epitaxy
MQWs	Multi-quantum wells
ND	Neutral density
OC	Output coupler
PH3	Phosphine
PL	Photoluminescence
PV	Photovoltaic
QD	Quantum dot
QE	Quantum efficiency
SEM	Scanning electron microscope
SRH	Shockley-Read-Hall
TDPL	Temperature-dependent photoluminescence
TCSPC	Time-correlated single-photon counting
TRPL	Time-resolved photoluminescence
TMG	Trimethylgallium
TMI	Trimethylindium
WZ	Wurtzite
ZB	Zinc blende

Table of contents

1. Introduction

The *semiconductor nanowire* is one of the nanostructures that has the potential to replace electrical devices with a conventional planar structure technology. It is a cylindrical semiconductor that has a diameter on a scale of nanometers with a length as long as a few micrometers. The nanowire has advantages over the conventional devices, especially in optoelectronics applications. The nanowire is also suitable for sensing applications where the surface is an active area due to a high surface-to-volume ratio of the nanowire. Figure 1-1 (a) is the scanning electron microscope (SEM) image of the nanowire sample studied in this work.

For example; an array of nanowires on the top of the photovoltaic (PV) cell (Figure 1-1 (b)) could increase the chance of light trapping. This in turn improves the device's efficiency significantly [1]. A nanowire growth with direct bandgap materials; e.g. alloys of group III and V in the periodic table, on cheap Si substrate (Figure 1-1 (c)) for the light emitting diode (LED) has higher cost efficiency [2]. Also, the nanowire can be used as a laser cavity (Figure 1-1 (d)) for an ultra-small laser diode (LD) [3].

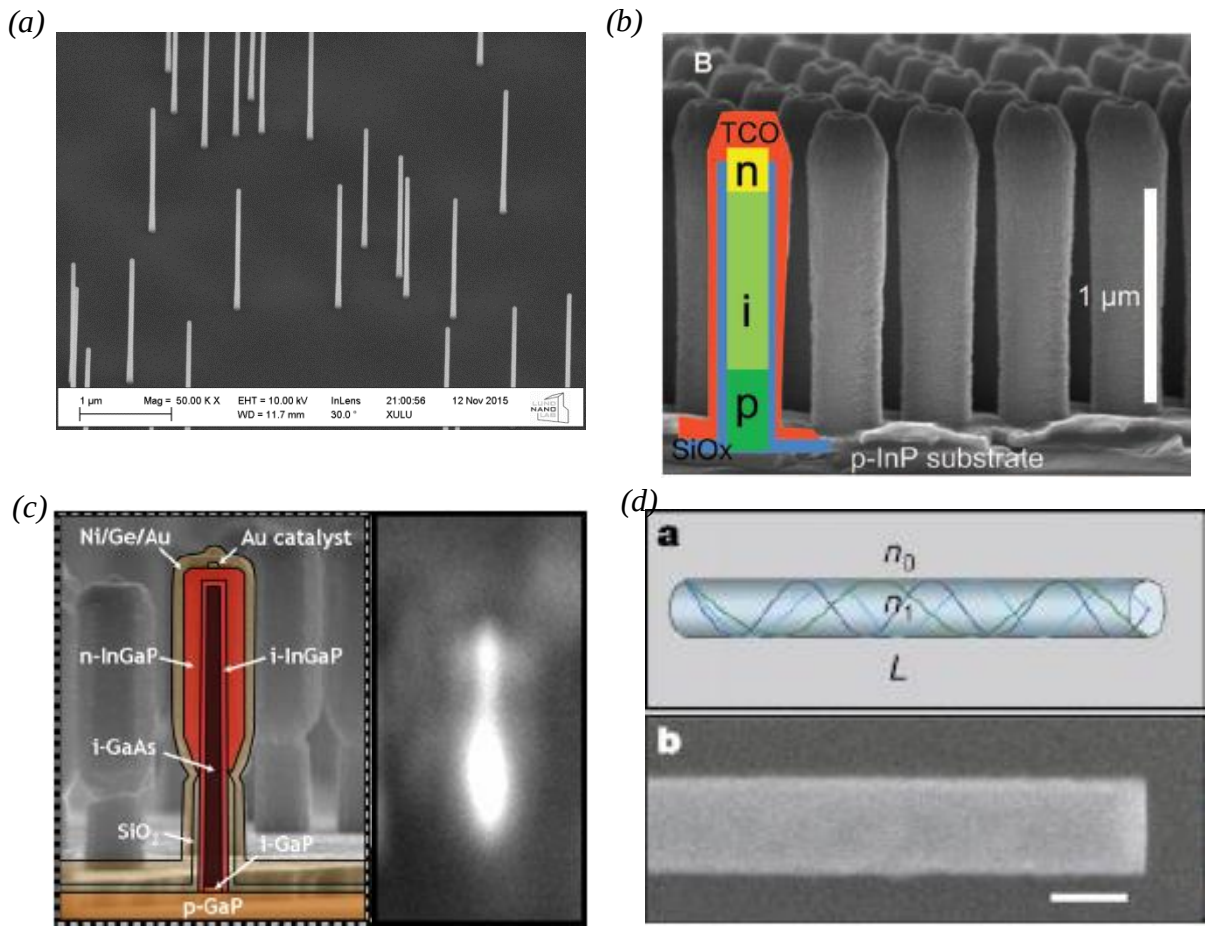

Figure 1-1: (a) An SEM image of nanowire sample studied in this work. (b) An array of nanowires for a photovoltaic (PV) cell with superimposed schematic illustrates compositions on nanowire. (c) The nanowire as LED. (d) A schematic of a nanowire as a laser cavity. (figure taken from ref. [1]on (b), ref. [2]on (c), and ref. [3]on (d))

1.1. Carrier recombination lifetime

In a semiconductor optoelectronic device, light absorption (emission) occurs when an electron-hole pair is created (recombined). The total rate of the concentration for both electrons (n) and holes (p) as a function of a generation and recombination rate is

$$\frac{dn}{dt} = \frac{dp}{dt} = G - R \qquad \text{eq. 1}$$

where G (R) is a generation (recombination) rate. At an equilibrium condition, the generation rate is $G = Bn_0p_0$ where B is the quantum-mechanical probability of a radiative transition [4]. n_0 (p_0) is the equilibrium concentrations of electrons (holes). Two major recombination mechanisms of the electron-hole pair are *radiative* and *non-radiative recombination*. The latter case can be separated into two sub-mechanisms: *Auger recombination* and *Shockley-Read-Hall (SRH) recombination*.

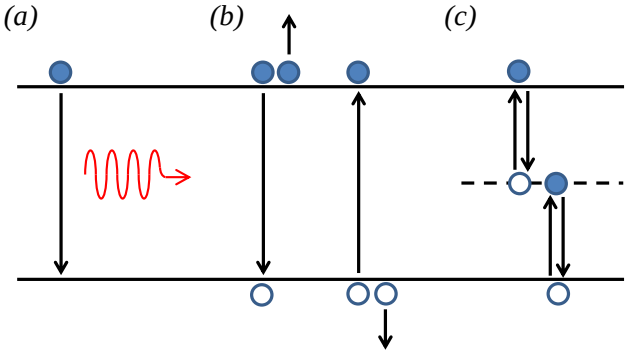

Figure 1-2: Schematic shows the basic recombination mechanisms, Radiation recombination (a), Auger recombination (b), and SRH recombination (c).

Radiative recombination: Upon recombination of an excited electron at the conduction band edge with a hole at the valence band edge, an excess energy is released as a photon, Figure 1-2 (a). This particular process most likely occurs in a direct bandgap semiconductor which is free from defects.

With an excitation which in this case is an external light source, the generation rate becomes $R_{rad} = Bnp$ where $n = n_0 + \Delta n$, and $p = p_0 + \Delta p$. Δn, and Δp are the concentration of injected electrons and holes regarding the photo generation. Due to the neutralization of photo generated charge carriers, the injected concentration can be estimated as $\Delta n = \Delta p$. By substituting the total concentration with equilibrium concentration and excess carriers, the recombination rate can be written as eq. 2. As the excitation source is turned off, the generation rate then returns to the equilibrium. The changing rate of the injected carriers is decreased as eq. 3.

$$R_{rad} = B(n_0 + \Delta n)(p_0 + \Delta p) = B\big(n_0p_0 + (\Delta n)^2 + \Delta n(n_0 + p_0)\big) \qquad \text{eq. 2}$$

$$\frac{d\Delta n}{dt} = -B\big((\Delta n)^2 + \Delta n(n_0 + p_0)\big) \qquad \text{eq. 3}$$

In the case of low-level injection (LLI), when the concentration of the injected carriers is much lower than the total equilibrium concentration, $\Delta n \ll n_0 + p_0$, the first term in eq. 3 can be omitted. The solution for eq. 3 with this assumption is an exponential function, $\Delta n(t) = \Delta n(t_0) e^{-(t-t_0)/\tau_{rad}^{LLI}}$ where time t_0 is the time that an injection source is suddenly removed and τ_{rad}^{LLI} is a radiative recombination lifetime. The lifetime in this case can be expressed as

LLI: $$\tau_{rad}^{LLI} = \frac{1}{B(n_0 + p_0)} = \frac{1}{BN_{dop}} \quad \text{eq. 4}$$

where $N_{dop} \equiv n_0 + p_0$ is the doping concentration. N_{dop} is considered as the concentration of the background charge carriers. Thus, the lifetime is an injection independent for the LLI case but depends on the doping concentration [4].

In contrast with high-level injection (HLI) case, the injected concentration of the charge carriers is larger than the total equilibrium concentration, $\Delta n \gg n_0 + p_0$. The first term of eq. 3 dominates. As a result, the solution gives the lifetime, τ_{rad}^{HLI}, as a linear decline function of the injected carriers as

HLI: $$\tau_{rad}^{HLI} = \frac{1}{B\Delta n} \quad \text{eq. 5}$$

Auger recombination: The excess energy of the recombination is given to a third carrier instead of the photoemission. The excess energy would then thermalize that third carrier from the band edge, Figure 1-2 (b).

Two mechanisms are distinguished regarding the third carrier that takes part in the Auger recombination process. They are electron-electron-hole (*eeh)* and electron-hole-hole (*ehh*) processes [4]. The excess energy is transferred to an electron within the conduction band for *eeh*-process. On the other hand, a hole would instead get the excess energy for *ehh*-process. The Auger recombination rate is written as

$$R_{Auger} = C_n(n^2 p - n_0^2 p_0) + C_p(np^2 - n_0 p_0^2) \quad \text{eq. 6}$$

where C_n and C_p are the coefficients of the *eeh*- and *ehh*-processes, respectively. In analogy to radiative recombination, the solution of the rate equation gives the lifetime of the Auger mechanism in both injection levels, LLI and HLI, as eq. 7 and eq. 8, respectively.

LLI: $$\tau_{Auger}^{LLI} = \frac{1}{C_n N_{dop}^2} \quad \text{eq. 7}$$

HLI: $$\tau_{Auger}^{HLI} = \frac{1}{(C_n + C_p)\Delta n^2} = \frac{1}{C_a \Delta n^2} \quad \text{eq. 8}$$

where $C_a \equiv C_n + C_p$ is called the ambipolar Auger coefficient.

Shockley-Read-Hall recombination: Instead of the direct recombination of the carriers at the band edge, there is a stepwise recombination with a transition state within the bandgap, Figure 1-2 (c). The rate of *SRH recombination* can be separated into two cases regarding the transition

states. The first one is the recombination through the transition state from defects and impurities within bulk material. There is a single energy level in between the bandgap [4]. Another process is through the transition states from dangling bond on the surface of the material. The energy levels of surface states are then distributed along the bandgap. The SRH recombination through the surface state is the dominating mechanism for the nanowire which has a large surface-to-volume ratio.

Unlike the previous two recombination mechanisms, an expression of SRH recombination rate is much more complicate because the process involves a number of variables. From Rein's lifetime spectroscopy book [4], the equation for SRH recombination lifetime is

$$\tau_{SRH} = \frac{\tau_{n0}(p_0 + p_1 + \Delta n) + \tau_{p0}(n_0 + n_1 + \Delta n)}{p_0 + n_0 + \Delta n} \qquad \text{eq. 9}$$

where τ_{p0} (τ_{n0}) are the capture time constants of holes (electrons). n_1, and p_1 are the carriers concentration at defects or impurities energy level.

From eq. 5 and eq. 8, the lifetime of the radiative and the Auger recombination at HLI is inversely proportional to the injection level. However, the relation between lifetime and the injection level is stronger for the Auger recombination. The lifetimes of both mechanisms are constant at LLI and decreases at HLI. These results are illustrated in Figure 1-3 as a plot between the recombination lifetime and the injection level. On the other hand, the lifetime is longer in HLI regime for the SRH recombination because it is proportional to $\tau_{p0} + \tau_{n0}$. At LLI, τ_{SRH} is proportional to τ_{p0} (τ_{n0}) for an *n* (*p*) doped semiconductor.

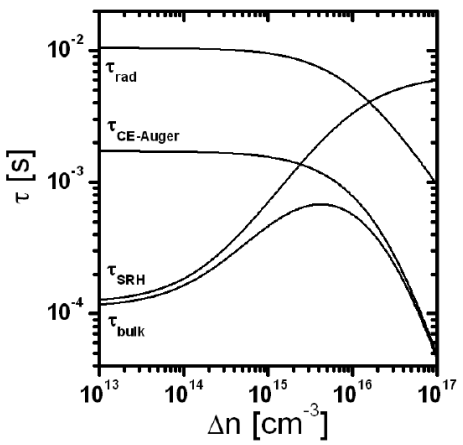

Figure 1-3: Plot of carrier lifetime vs. injected carrier concentration for sillicon. (taken from ref [5])

The total recombination rate is the sum of the radiative, Auger, and SRH recombination rates. The total lifetime can, therefore, be expressed as:

$$\frac{1}{\tau} = \frac{1}{\tau_{rad}} + \frac{1}{\tau_{nr}} = \frac{1}{\tau_{rad}} + \left(\frac{1}{\tau_{Aug}} + \frac{1}{\tau_{SRH}}\right) \qquad \text{eq. 10}$$

where τ_{nr} is the non-radiative recombination lifetime.

1.2.Nanowire heterostructures

A typical process used for nanowire growth is Au-assisted metal-organic vapor phase epitaxy (MOVPE). The process starts with a deposition of Au aerosol particles on a substrate. These Au particles on the substrate act as nucleation sites which collect group III and V elements from a gaseous phase. As the materials subsequently accumulate at the Au-semiconductor interface, a nanowire is formed underneath the Au particle. The size of the nanowire depends on the size of the Au particle. The particular crystal structure of the nanowire can be achieved by controlling growth conditions such as temperature, and the amount of precursors.

By changing the composition of the gas flow during the growth process, nanowire heterostructures can be created. The heterostructure can be undertaken in both directions of the wire as an *axial heterostructure* or a *radial heterostructure*. The axial nanowire heterostructure has a different material along the nanowire growth direction. It is the result of the changing in precursor gas flow during the growth process. In the conventional planar technology, strain can be induced on the heterostructure due to a different lattice constant of materials. However, strain in axial heterostructures can be relaxed radially due to the small lateral dimension of the nanowire. Therefore, nanowire heterostructures can be created from various material combinations which are not possible in conventional planar epitaxial fabrication. For the radial nanowire heterostructure, the different material (shell layer) is grown radially to cover the side facet of the previous growth nanowire (core nanowire). This configuration of the nanowire is called core-shell nanowire.

With the core-shell nanowire, there is a band offset between the core nanowire and the shell layer. It is possible to control where the charge carriers recombine with the band offset. The carriers from the larger bandgap of the shell layer are swept toward the lower bandgap region of the core nanowire. Consequently, the carriers move from the shell into the core nanowire, Figure 1-4. More carriers within the core nanowire increase the chance of radiative recombination. Also, the effect of the surface SRH recombination could be reduced as the carriers are also allocated away from the surface. The shell is used to passivate the surface states which are the most detrimental non-radiative recombination centers. This method is called *surface passivation*, which is one of the methods to improve the performance of the nanowires.

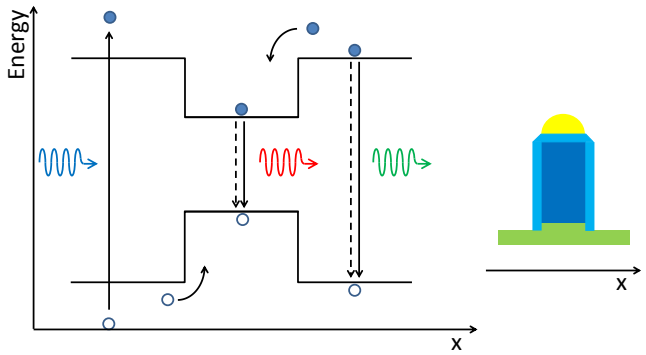

Figure 1-4: Band structure of core-shell nanowire with the possible transformation of the carriers. The left most up arrow represents an excitation from absorbed photon. The solid and dashed lines are radiative and non-radiative recombination, respectively.

1.3. Internal Quantum Efficiency (IQE)

One of the parameters describing the performance of the optoelectronic devices is the *internal quantum efficiency* (IQE, η_i). It is defined as the ratio between the radiative recombination rate, R_{rad}, and the total recombination rate, R. Because the recombination rate is inversely proportional to the recombination lifetime, the IQE can be expressed in terms of the lifetime as eq. 11 [6].

$$\eta_i = \frac{R_{rad}}{R} = \frac{\tau}{\tau_r} \qquad \text{eq. 11}$$

This work aims to perform a *time-resolved photoluminescence* (TRPL) study on ternary (InGaP) alloy nanowires to improve the IQE. By measuring the TRPL with the LLI condition, the total lifetime (τ) is the measurement result, and the radiative recombination lifetime (τ_{rad}) is constant regarding the doping concentration. Therefore, the denominator of eq. 11 would then be constant, as a result, the IQE would be implicitly determined. The measurements were performed on both plain nanowires and core-shell nanowires. As a result of the surface passivation, the performance of the core-shell nanowires is expected to be better than the plain nanowires.

Prior to the TRPL measurement, the *photoluminescence (PL) spectroscopy* was used to evaluate the band offset between the shell layer and the core nanowire. The measurement is to assess the core-shell nanowire with the proper condition of the surface passivation. Then, the *temperature-dependent photoluminescence* (TDPL) which is the PL spectroscopy at different temperature was performed to investigate an energy structure of non-radiative recombination centers.

2. Methodology

2.1. Sample preparation

Because this work did not focus on the nanowire growth processes, this section briefly describes the preparation method of nanowire samples. The samples for these studies consist of plain nanowires and core-shell nanowires.

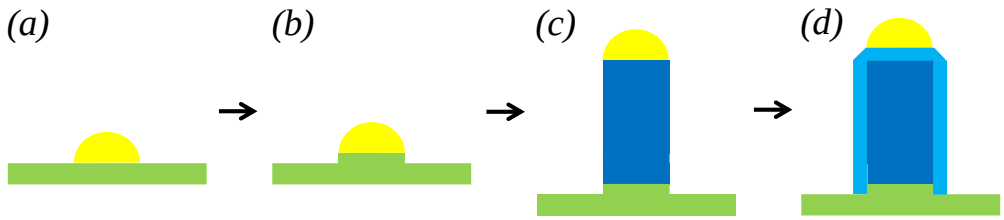

Figure 2-1: (a) A deposited Au particle on the substrate, (b) A small portion of stub, (c) InGaP nanowire growth, (d) The core-shell nanowire as the radial heterostructure.

The nanowire growth with the Au-assisted MOVPE process started with a feeding of Trimethylindium (TMI) and Phosphine (PH_3) precursors. These two precursors decomposed into Indium (In) and Phosphor (P), respectively, at the Au particle. The In and P subsequently were accumulated underneath the Au particles on the substrate. This portion of the nanowire is called the InP stub, Figure 2-1 (b). The stub portion would help the further growth of the ternary alloy nanowire on the substrate because the stub acts as a strain relief layer between the substrate and the nanowire. After completing the desired portion of the stub, Trimethylgallium (TMG), which decomposed into Galluim (Ga), was fed into the growth chamber in addition to the TMI and PH_3. These three elements then formed the InGaP nanowire, Figure 2-1 (c). These plain nanowires were a primary sample used in this study.

For the synthesis of the shell layer, the growth temperature was subsequently increased after finishing the growth of the core nanowire. The higher temperature gives a sufficient thermal energy for the precursors to deposit on the side facets of the wire. With this condition, the radial growth is more favorable. Consequently, the core-shell nanowire could be achieved, Figure 2-1 (d). The shell had the same alloy materials as the core nanowire but different compositions. In order to study the effect of the shell composition on the lifetime of the core luminescence, the TMG gas flow in the growth process was varied to change the Ga composition of InGaP shell. With the TMG gas flow of the core nanowire growth as a reference, 3.4 sccm, there were four different flows for the shell growth as 1 sccm, 2.2 sccm, 3.4 sccm, and 4.4 sccm. The core-shell nanowire samples have three different core diameters which are 16 nm, 20 nm, and 40 nm. The shell thickness, 8 nm, is the same for every nanowire.

The nanowires were then gathered from the substrate by a piece of cleanroom paper rubbing on top of the substrate. Each type of nanowire was transferred to different substrates, which have a pattern of a coordinate system. After the transferring, they were randomly laid down on top of the new substrate. The coordinate system was then used to locate a particular nanowire for further investigations.

The patterned substrate with the nanowires was held on the cryostat cold finger by using silver glue. This is a special kind of glue that has a heat conductive property. The cold finger was connected to a thermocouple that can monitor and control the temperature. Therefore, it was possible to perform the TDPL measurement. The sample stayed within the cryostat chamber which connected to the pressure pump and a He tank. The condition for the samples within the chamber was roughly about $10^{-5}\ Pa$ for the pressure and $4\ K$ for the temperature.

2.2. Measurement setup

There were two types of measurements, PL measurements, and TRPL measurements, performed in this work. The difference between these two measurements was the light source and the detector; otherwise, the rest of the setup was the same. For the PL measurement, the light source was a continuous wave (CW) Nd:YAG laser, and the detector was a charge-coupled device (CCD) camera. The TRPL measurement had a Ti:Sapphire pulsed laser as the light source, and an Avalanche photodiode (APD) as the detector.

Figure 2-2 shows a schematic of the overall setup. The excitation light entered the setup via an optical fiber and a fiber collimator. The light then passed two beam splitters (BS1 and BS2). At BS1, part of the beam went to an objective lens and focused onto a particular nanowire. The remaining of the laser beam from BS1 would go to the power meter. Hence, it was possible to monitor the power of the excitation light. The same objective then collected the luminescence and sent it through BS1 towards the spectrometer. The reflected laser from the samples was blocked by a long pass filter, which filters the different wavelength depending on the light source used for each measurement. At this point, only the luminescence from the sample could

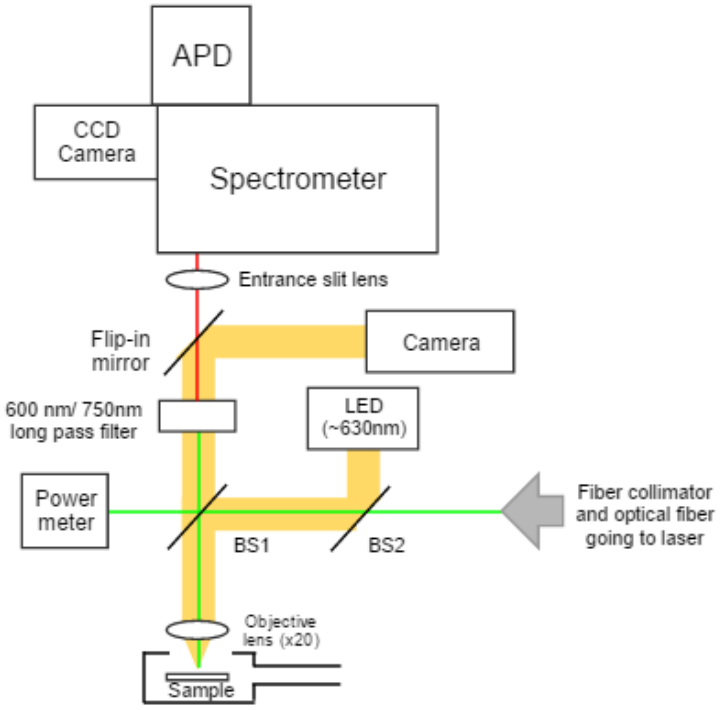

Figure 2-2: The diagram shows the common setup of PL measurement and TRPL measurement where the green and the red line represent the light from the laser source and the luminescence from the sample, respectively.

reach the spectrometer. Within the spectrometer, the luminescence light was dispersed by the grating and it was collected by either the CCD camera or the APD depending on the position of a flip-in mirror within the spectrometer. To image the sample and find the wire for the measurement, LED was used for illuminating a large area. The reflected LED light was sent to a small camera via another flip-in mirror. The LED and the camera worked together with the objective lens as a microscope.

2.2.1. Photoluminescence (PL) measurement setup

The light source for the PL measurement in this study is a Nd:YAG laser that can generate a coherent CW light with the wavelength of 532 nm. To control the laser light power, there were several neutral density (ND) filters along the beam path before the laser light was coupled to a fiber waveguide. The ND filter with optical density d reduces the intensity of the light by the same amount regardless of the wavelength with the transmission of 10^{-d}. The fiber was connected to the setup as shown in Figure 2-2. Inside the spectrometer, there is a grating which disperses the light along the horizontal axis onto the CCD camera. Therefore, each pixel on the horizontal plane of the camera represents the different wavelength of the light.

2.2.2. Time-resolved photoluminescence (TRPL) measurement setup

The measurement is performed to investigate time-dependent behaviors of the photo-generated carriers which have been created within a short period of time. There is only a certain amount of carriers excited by the laser light. For this purpose, a mode-locked Ti:Sapphire pulsed laser was used. The laser can provide pulses as short as 100 fs with a pulse frequency of 80 MHz. The wavelength from this laser is tunable between 730 and 950 nm. It is pumped by a Nd:YAG laser.

2.2.2.1. Laser pulse mode-locking

The principle of the mode-locking is to lock the phase of many longitudinal modes oscillating independently within a laser cavity. As a result, a short pulse of a laser light is created. There are two methods of the mode locking, an active mode locking and a passive mode locking. They are distinguished by an external signal for the pulse modulation. For the active mode locking laser, there is commonly an acousto-optic or electro-optic switch located within the laser cavity. The switch turns on, whereupon the pulse gets across. The pulse is created when longitudinal modes with the same phase are combined. The other combination of out-of-phase modes is blocked by the switch. Pulse duration is shortened regarding the number of frequencies locked together, and it can be determined from Fourier's transform of those frequencies: the broader frequency range of the light spectrum, the shorter the pulse duration.

In this work, the Ti:Sapphire laser used for the measurement is the *Tsunami Models 3941* which operates with the active mode-locking. The acousto-optic modulator (AOM) was used as a switch, and it was in front of output coupler (OC), Figure 2-3. To select the output wavelength and adjust the pulse duration, prisms (Pr2, and Pr3) and tuning slit needs to be adjusted, Figure 2-3. A set of prisms spatially disperses the light and determines the pulse duration. The slit is adjusted to pick up a specific wavelength. Therefore, by optimizing those components, a proper wavelength and a pulse duration for the measurement can be achieved.

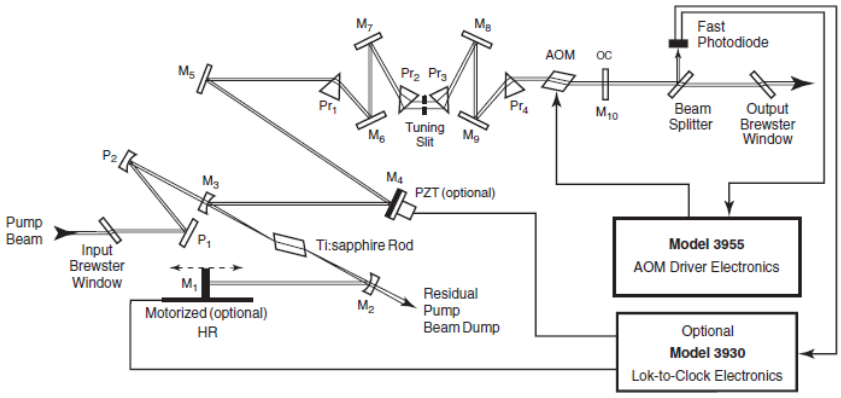

Figure 2-3: A schematic of optical components and a beam path within Tsunami Models 3941 Femtosecond laser used as a light source of time-resolved PL measurement. The schematic is from the laser user's manual.

2.2.2.2. Time-resolved photoluminescence detectors

An avalanche photodiode (APD) is another kind of photodetector which can detect weak signals through the process of impact (avalanche) ionization. This means the APD is sensitive enough to register single photon events. With a strong electric field applied inversely to the *p-n* junction of the APD, the photogenerated electron-hole pair is accelerated and attained a higher kinetic energy. They collide with a lattice, point 1 in Figure 2-4, creating the second electron-hole pair by impact ionization. Those electrons are continuously accelerated under the electric field which will then create more electrons, point 2 in Figure 2-4. It is the same for the holes created within the valence band, but they travel in the opposite direction, point 3 in Figure 2-4. Consequently, a single photon can create a large number of charge carriers; i.e. stronger signal, through this amplification process.

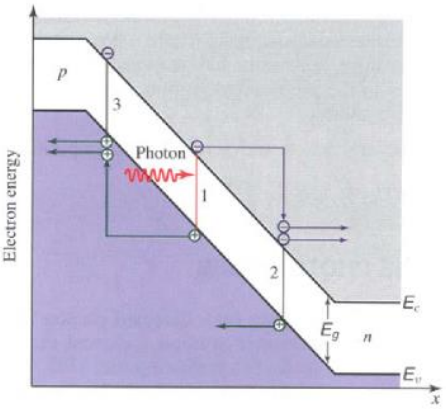

Figure 2-4: A schematic illustrates the mechanism of impact ionization within APD.(taken from ref [6])

The technique called *Time-Correlated Single-Photon Counting (TCSPC)* was used with the APD to measure the time-resolved PL. There is a certain amount of electrons from the photogeneration process, especially with the pulse laser. They would then be recombined with the holes as an exponential decay explained in Section 1.1. However, the APD can only pick up a single photon at the certain time of those recombination processes. Then, it takes a while to get another photon from the later photo event. The signal of the photons labeled with their arrival time is stored in the computer memory. It takes a period of time to accumulate the data to build up a histogram representing the decay waveform as Figure 2-5.

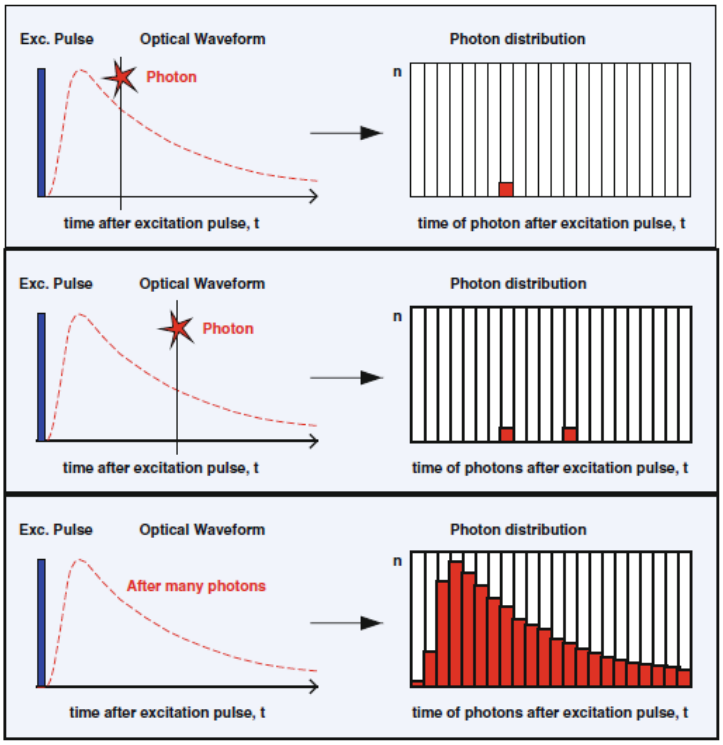

Figure 2-5: The build-up of photon distribution over pulse period from each excitation in TCSPC.(taken from ref [8])

The measurement period need to be the inverse of the laser pulse frequency. To achieve this, the sync signal from the photodiode inside the laser was used to operate the APD. That signal would have the same frequency as the laser pulse. The frequency of the signal is also another limitation of the measurement. The system has about 12 ns (1/(80 MHz)) time window for the decay. If the decay is longer than that time window, the amount of the photo generated carriers will be affected by the previous excitation pulse.

The dispersed light arising from the spectrometer was collimated and focused on the APD. The model of the APD used in these studies is *SPCM-AQR 16.* The critical matter of this specific model is that the light needs to be focused exactly on the active region of the APD.

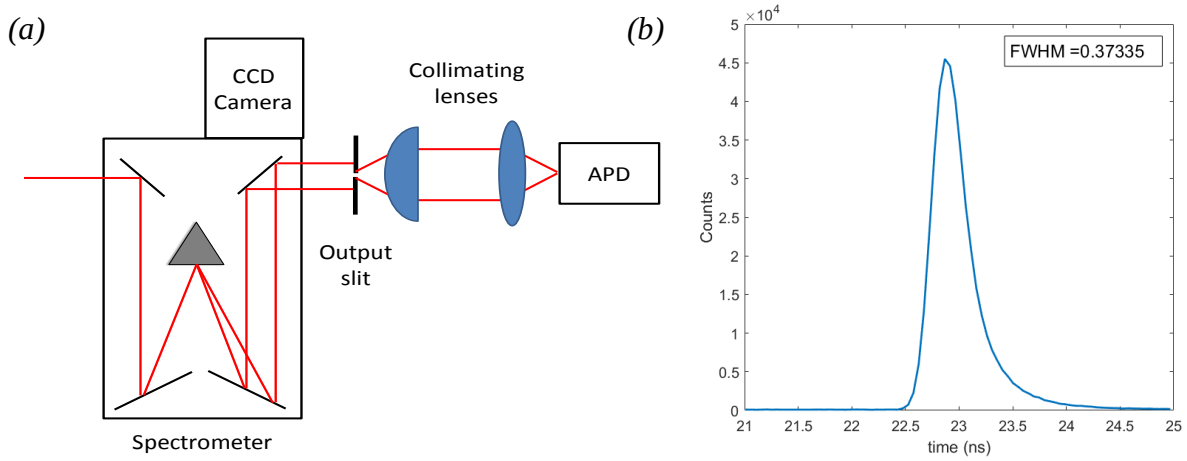

Figure 2-6: (a) The APD setup at the second output port of the spectrometer. The collimating lenses used to collimate dispersed light from the spectrometer and focus on the APD. (b) The laser pulse measured with the APD after passing through the spectrometer. The pulse has the FWHM about 370 ps.

Otherwise, the measurement result could be affected by the diffusion of the excited carriers from an inactive region. Those carriers would diffuse into the active region and contribute to their own decay process. Consequently, the lifetime measured from the sample would then be affected by the detector.

This APD has the time resolution of 350 ps for the single photon count and the quantum efficiency of 55 - 65% at 830 nm. The APD was used to measure the direct laser pulse to ensure that the equipment had a sufficient temporal resolution for the TRPL measurement. The result gave the pulse duration at full-width-half-maximum (FWHM) about 370 ps which is almost the same as device's resolution. In conclusion, the APD setup is good for the TRPL measurement.

Another time-resolved photoluminescence detector is the streak camera which is a widely used device for the TRPL measurement with a temporal resolution down to a few picoseconds (~1 ps). The principle of the measurement is to convert the photon flux into an electron flux by a photocathode. The electrons are accelerated and focused into deflection couple plates. They are deflected with an electric field according to their arrival time, Figure 2-7. Therefore, the temporal distribution of the light pulse is transformed into a vertical spatial spreading. Later, it is converted back again to the photon flux by a phosphorus screen and captured with a CCD camera. Although it has a good temporal resolution, the device's quantum efficiency (QE) is very low (<1%) in the studied wavelength range (800-900 nm), Figure 2-8. In this work, an already existing streak camera set-up was used for some initial measurement.

For the streak camera, the sample needs to be excited with higher laser power to get a sufficient luminescence signal, so the luminescence can only be studied on the HLI regime. Therefore, the APD which has the lower temporal resolution but higher QE was selected for the measurement instead. It is expected to get an adequate signal for the TRPL within the LLI regime for the IQE studies as mentioned in Section 1.3.

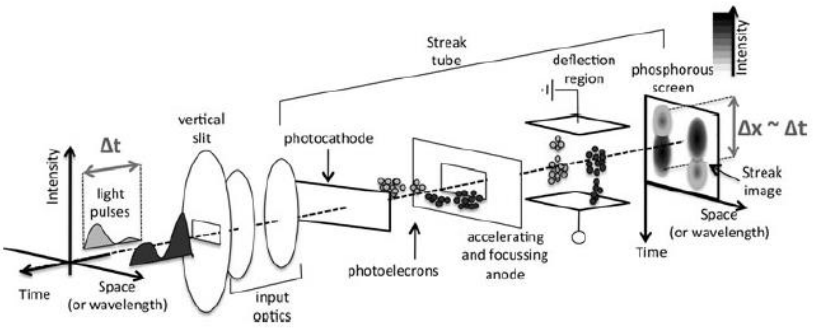

Figure 2-7: A schematic of light pulse transformation on to phosphorous screen.(taken from ref [9])

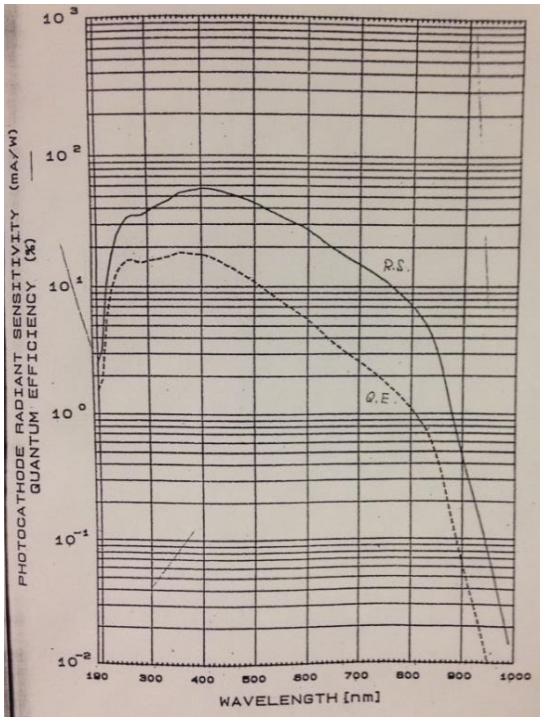

Figure 2-8: The plot illustrates the performance of streak camera at Photoluminescence Laboratory, Solid State Division. The solid line is a radiant sensitivity (R.S.), and the dashed line is the quantum efficiency (Q.E.) of the photocathode.

3. Results and Discussions

3.1. Photoluminescence (PL) spectroscopy

3.1.1. PL Spectrum of plain nanowire

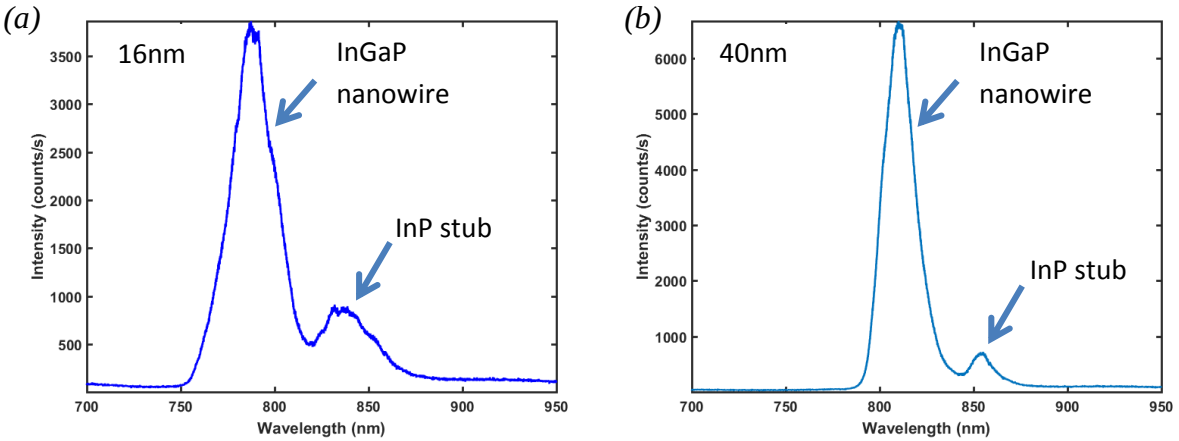

Figure 3-1: The PL spectrum of the plain nanowire with a diameter of 16nm (a), and 40nm (b).

The spectrum of the samples is shown in Figure 3-1 (a) and (b). They correspond to nanowires with the different diameters which are 16 nm and 40 nm, respectively. We observed two distinct peaks on the PL spectrum from these samples. The highest peaks are from the InGaP portion of the nanowire, and the smaller peak are from the stub, Figure 3-2 (b).

In order to evaluate the composition of the InGaP nanowires, a model for the relation between Ga composition and PL spectral peak is needed. Figure 3-2 (a) shows an estimation of that relation for Zinc blende (ZB) and Wurtzite (WZ) crystal structure. The estimation was adapted from *Olsen et al.* [10] which expressed the relation between the bandgap energy and the material composition of ZB InGaAsP at the room temperature. The relation of InGaP can be calculated as the composition of Arsenic (As) approaching zero. Then, the band gap energy was converted to the light wavelength at the temperature of 5 K. Consequently, the blue trace in Figure 3-2 (a) could be achieved.

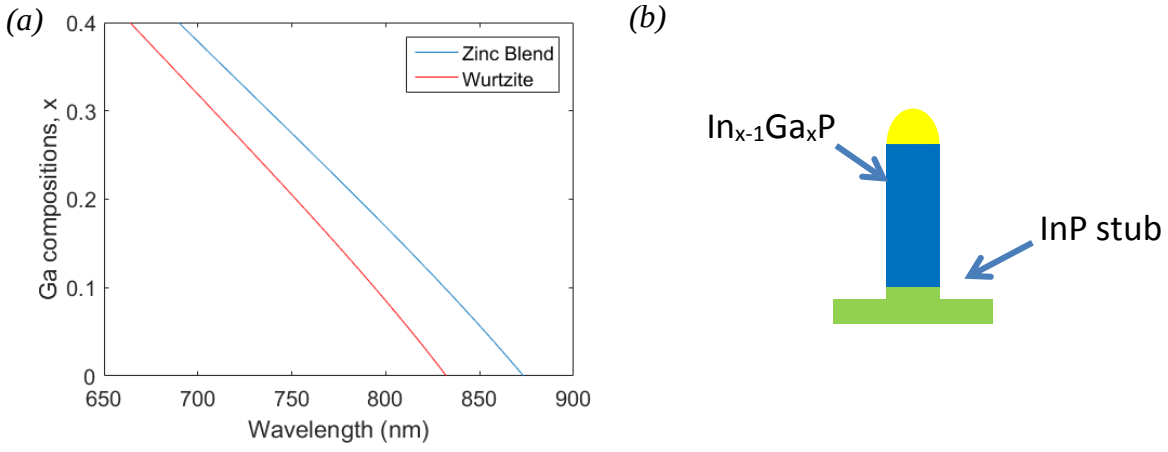

Figure 3-2: (a) A plot of PL wavelength from InGaP as a function of Ga compositions. (b) A schematic of the plain nanowire with a portion of InP stub and InGaP

Despite a non-preferable growth condition to any crystal structures, it is possible to have the WZ crystal structure on the nanowire. According to *Mishra et al.*[11], WZ InP nanowire has a bandgap energy which is about 40 nm (80 meV) above the bandgap energy of ZB. Assuming that this is also valid for InGaP nanowire, a WZ composition curve could be plotted as a red trace in Figure 3-2 (a). Where the Ga compositions x equals to 0, the emitted light from InP have a wavelength of 832 nm for WZ and 873 nm for ZB.

The wavelength (λ) of the light emitted from the semiconductor material represents, to a first approximation, by the bandgap energy (E_g) according to $E_g = hc/\lambda$, where h is Planck's constant and c is the speed of light. The approximation disregards the fact that the emission can be slightly below the bandgap due to doping levels. Those wavelengths are equivalent to the bandgap energy of 1.49 eV, and 1.42 eV, respectively. The PL spectrum results of both InP stub and InGaP nanowire can vary between the blue and the red trace in Figure 3-2 (a), depending on the crystal structure of the nanowire.

For the 16nm wire, the InGaP peak appears at 787.4 nm (1.576 eV) which corresponds to a Ga content of 0.11-0.19 according to Figure 3-2 (a). For the 40 nm wire, the InGaP peak has red-shifted to 810.1 nm (1.531 eV). The shift due to confinement is thus 45 meV. This is in reasonable agreement with a simple infinite well calculation which gives a red-shift of 30 meV as increasing the diameter from 16 nm to 40 nm.

3.1.2. PL spectrum of core-shell nanowires with different Ga composition

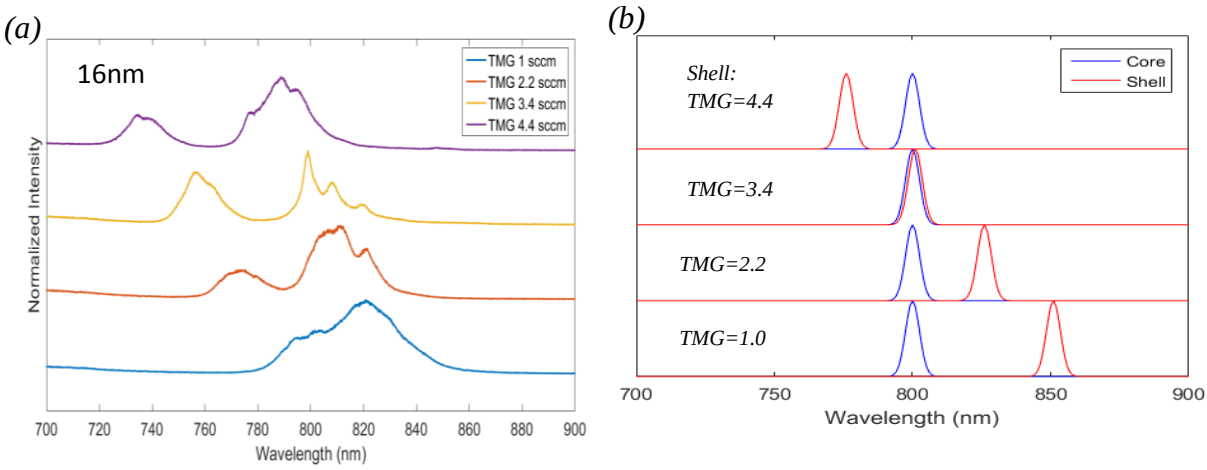

Figure 3-3: (a) A PL spectrum from the core-shell nanowires with a core diameter of 16 nm. (b) A schematic of an expected outcome of varying shell composition where the peak of the core (TMG=3.4 sccm) is at 800 nm but the peak of the shell is shifted regarding the variation of TMG.

The PL spectra from the 16 nm core nanowires with the variation of the shell composition are shown in Figure 3-3 (a). The PL spectra have two distinct peaks in every case except the one with the shell composition of TMG = 1 sccm. Figure 3-3 (b) is a schematic of expected spectra from the core-shell nanowires. The estimated peak positions in this schematic are not exact. The expected PL spectrum of core-shell nanowire regarding their composition should have one peak from the core and one from the shell. The luminescence of the core

nanowire is expected to be located at about 800 nm according to an average peak position of plain nanowire's spectra (Section 3.1.1). The shell luminescence expected to be varied around the core spectrum, as shown in Figure 3-3 (b), depending on its composition. It supposes to have only a single peak in the case that the core and the shell have the same material composition (TMG = 3.4 sccm). That means both of them have the same band gap, and hence the same luminescence wavelength. Therefore, the PL spectra mostly deviate from the expected result.

Despite the different growth processes, the actual material compositions are evidently different between the core nanowire and the shell layer. The growth process of the shell layer has the same mechanism as typical epitaxy growth process, but there is an involvement of Au particle for the nanowire growth. This can give different incorporation rates for the axial and the shell growth. Therefore, these could be the reason that the spectrum has two peaks when the TMG gas flow is the same between the core nanowire and the shell layer.

Both spectral peaks need to be identified with their source of luminescence which are either the core nanowire or the shell layer. In order to evaluate those spectra, an individual spectrum from the core and the shell was used as a reference. The PL result of the plain nanowire in section 3.1.1 is the reference for the core nanowire (blue traces in Figure 3-4). Because it is not possible to create the shell layer separately, the core-shell nanowire with a very thick shell (50 nm) was used as the reference for the shell layer. It is because, with the thick shell, most of the luminescence would come from the shell layer. The spectrum of this reference is red traces in Figure 3-4. The comparison was performed on the 16 nm and the 40 nm core nanowires. It shows that the left peak is the PL spectrum from the passivate shell layer, and the right peak is from the core nanowire. These are important information to keep in mind for further investigation of the core-shell nanowire.

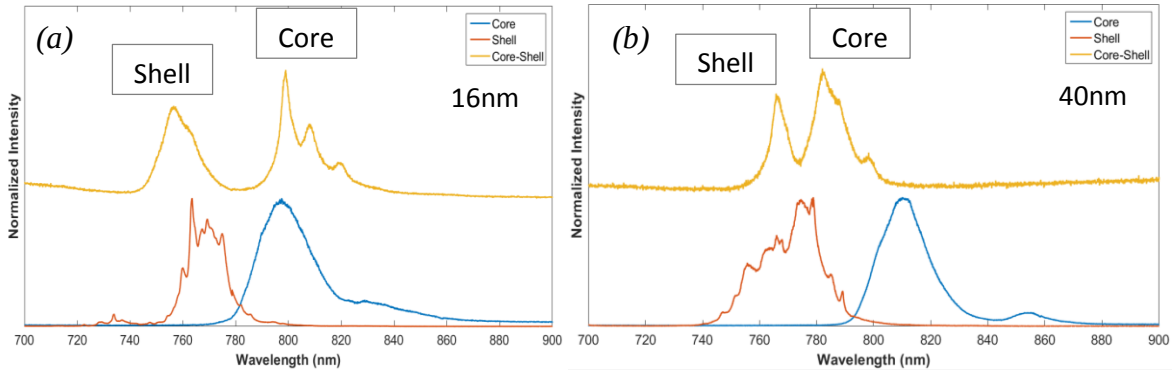

Figure 3-4: The comparison between PL spectrum from individual core/shell and core-shell nanowire with the diameter of 16 nm (a) and 40 nm (b) with a TMG gas flow of 3.4 sccm.

All the core-shell nanowires displayed two distinct peaks in their spectra. Figure 3-5 (a), (b), and (c) show the average peak positions for the core-shell nanowires with 16, 20, and 40 nm core diameters as a function of TMG flow. Each point on the plot is an average peak position, and the error bars are a standard deviation of each measurement result. Blue lines in plots of Figure 3-5 illustrate the average peak position of the shell's spectrum varying in between 740 nm to 800 nm. They are all in the same range for the different core diameters. This is another evidence to ensure that the spectrum at the low wavelength is from the shell because they all have the same thickness. Even the compositions of the shell were changed; its spectra from the different core diameter are still consistent. On the other hand, the average peak positions of the core (red line) are varying from one case of the core's diameter to the others.

There are two unexpected observations from this mean peak position plot (Figure 3-5). First, the core's peak position is supposed to be at the same wavelength for every TMG flow, because they all have the same material composition. In other words, the red lines should be horizontal. However, the red curve shifts toward the shorter wavelength, blue-shifted, as an increasing of the Ga composition in the shell. The suspected cause of this phenomenon is a strain effect due to the lattice mismatch between the core and the shell. Because of the different material compositions between the core and the shell, they have the different lattice constant

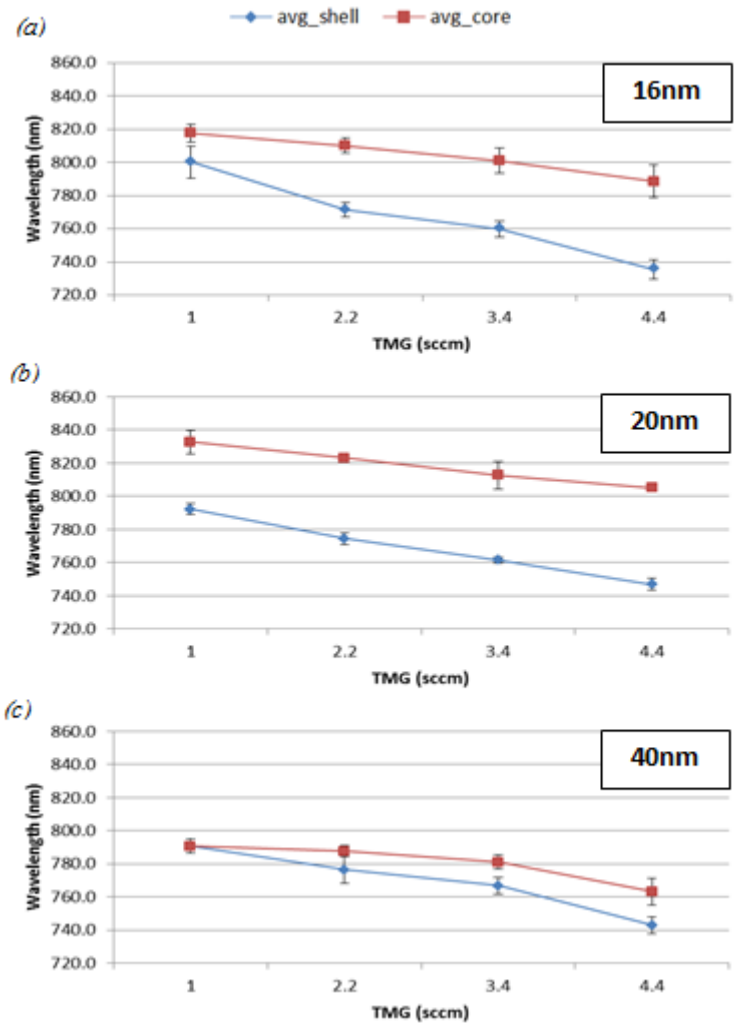

Figure 3-5: The peak position of core and shell PL spectrum at the different TMG flows with core diameters of 16 nm (a), 20 nm (b), and 40 nm (c).

which can induce strain on the core nanowire. The strain also affects material's bandgap, and hence the PL spectrum.

The second observation is the shifting of the core's peak position between the different cases of the core's diameter. From 16 nm to 20 nm nanowires, the overall range of the core's peak position is red-shifted as the result of the confinement. The effect of the confinement had already been discussed earlier between the PL spectrum of 16 nm and 40 nm plain nanowire. On the other hand, it is blue-shifted as the core diameter increases from 20 nm to 40 nm nanowire. If the blue-shifted is really an effect from the strain as mentioned earlier, the 40 nm core-shell nanowire would then be affect by strain rather than the confinement. This is not an expected outcome because the strain should be larger in the thinner wires. For this reason, it cannot be definitely concluded that the low energy peak in the case of 16 nm and 20 nm nanowires actually come from the core. It could also be related to the stub because those spectra are close to the position of the stub spectra.

To conclude this section, the core-shell nanowire samples could be successfully created with the bandgap of the shell larger than the core. It is a fulfilled condition for the surface passivation. However, the lattice mismatch can also generate dislocation defects on an interface between the core and the shell, Figure 3-6, which is considered as the center of non-radiative recombination. Further study need to be conducted in order to investigate the red/blue shift effect between the different core's diameters.

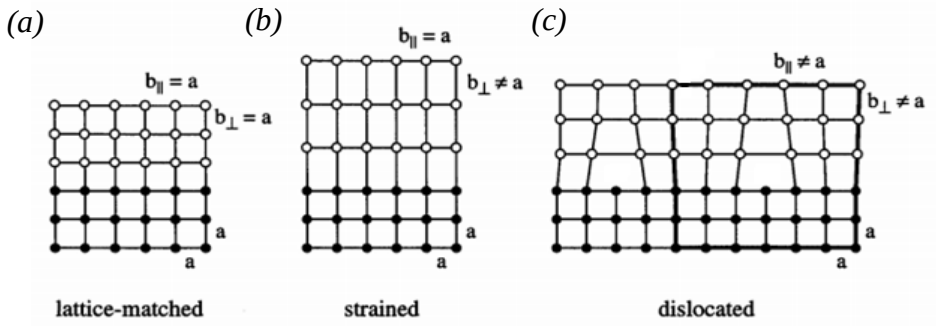

Figure 3-6: (a) Lattice matched between the substrate and the growth layer. (b) Lattice mismatched where the strain occurs on the growth layer as a misshaped crystal structure. (c) the strain is relieved by the dislocation of atoms in the crystal structure as a defect within an interface.(take from ref [12])

3.2. Time-Resolved Photoluminescence (TRPL)

3.2.1. TRPL Measurements of Bulk Reference Samples

The TRPL measurements were first performed on InP bulk substrates to use their lifetimes as a reference for a sample free from non-radiative recombination centers. In addition, these measurements were used to test the newly built time resolved set-up with the APD during the project. There are two doped bulk samples with different doping materials which were Fe, and Zn. Zn doping ($N_A \approx 10^{18} cm^{-3}$) makes the semiconductor highly p-type. Fe doping ($N_A \approx 10^{7} cm^{-3}$) is used as a so called compensation doping. It compensates for the natural n-type doping in the InP wafer. A compensate doped material therefore makes the InP electrically neutral.

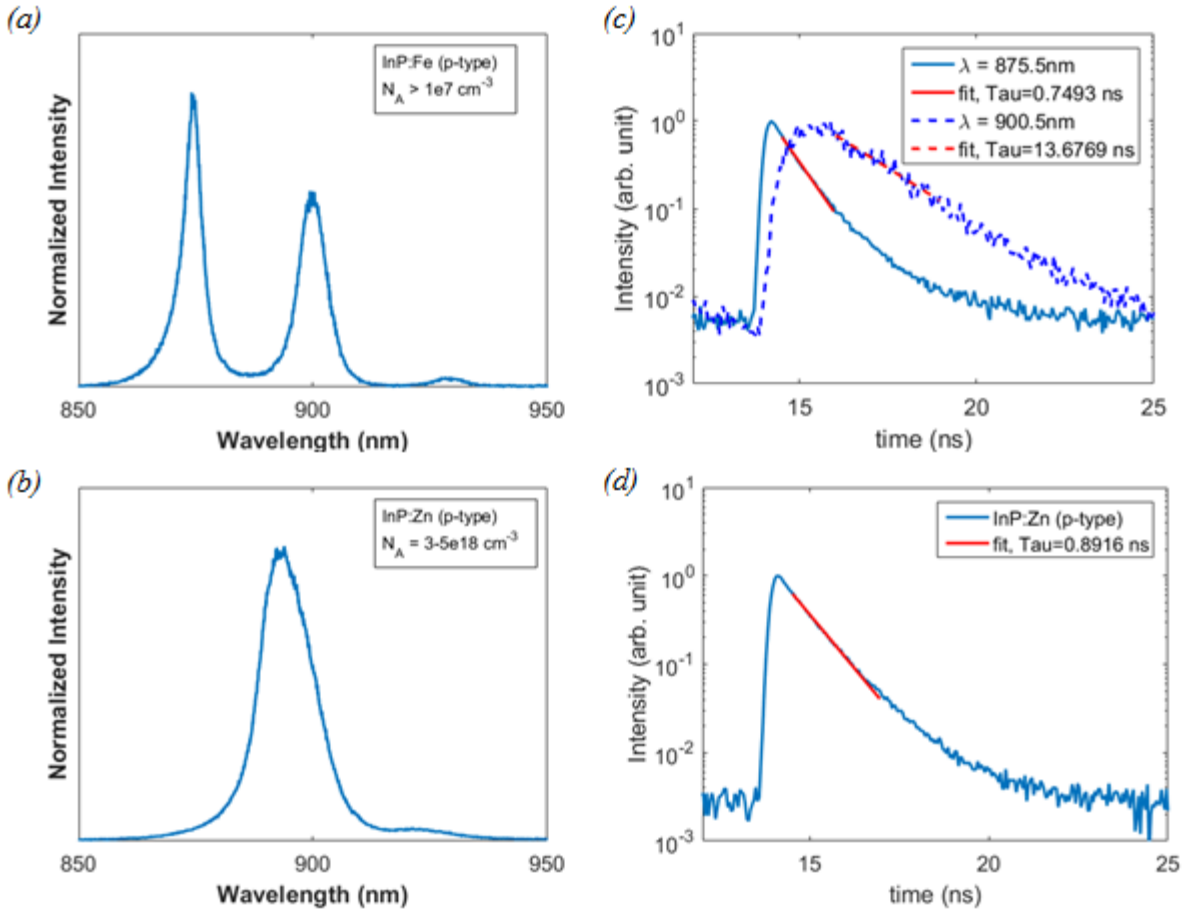

Figure 3-7: (a), and (b) are the PL spectrum of InP bulk substrate with Fe, and Zn-doped, respectively. (c), and (d) are the TRPL with a fitting line in red for the lifetime calculation. Since there are two peaks occurred in (a) for the Fe-doped sample, there are also two TRPL in (d)corresponding to each peak; i.e. the thick line for the peak at 875.5 nm and the dashed line for the peak at 900.5 nm.

There are two peaks from the Fe-doped sample, Figure 3-7 (a) which have two different lifetimes as 0.76 ns for the peak at 876 nm (thick line), and 13.7 ns for the peak at 901 nm (dashed line). The peak at the shorter wavelength corresponds to band-to-band recombination of the InP semiconductor. The other peak indicates the recombination through an energy level of the Fe doped inside the InP's bandgap. The short lifetime of Fe doped is roughly the same as the lifetime of the Zn-doped sample (0.89 ns), Figure 3-7 (d).

Because the Fe energy levels act as traps, the excited carriers would be trapped in this state before recombination. The energy level of the Fe-doped is closer to the band edge of the host semiconductor, so it cannot be considered as the non-radiative center which would be an energy level near the middle of the bandgap. The recombination with the trapping state therefore makes the lifetime longer than the other. The recombination of the Fe-doped sample is limited by the recombination process with the longest lifetime. Also, the plateau indicates the carrier's transformation from the larger band gap material to the narrower one as observed by *Trägårdh* [13].

Ideally, the reference samples should be an undoped bulk InP since a highly doping level affects the lifetime of the material (see Section 1.1). For this reason, the Fe-doped

sample is used as a reference for the nominally undoped bulk sample. The lifetime result of Zn doped could not be used as a reference because the sample is a highly doped material. Therefore, the long lifetime (13.7 ns) of this Fe doped InP was taken as a rough estimation of a sample free from non-radiative recombination centers. The lifetime of the nanowires should thus be compared to 13.7 ns.

3.2.2. TRPL Measurements of Nanowires

Following the characterization above, measurements were performed on the plain nanowire with two different diameters, 16 nm, and 40 nm. As a result, the lifetimes of the 16 nm and the 40 nm nanowire, Figure 3-8, are 4.8 ns and 6.2 ns, respectively. The lifetime of the 16 nm nanowire is presumably shorter than that of the 40nm nanowire due to the higher surface-to-volume ratio of the thinner nanowire. The lifetimes attained here are in the same range as the results of *Pemasiri et al.* [14] which applied the same excitation on the InP nanowire but whose measurements were performed with a streak camera.

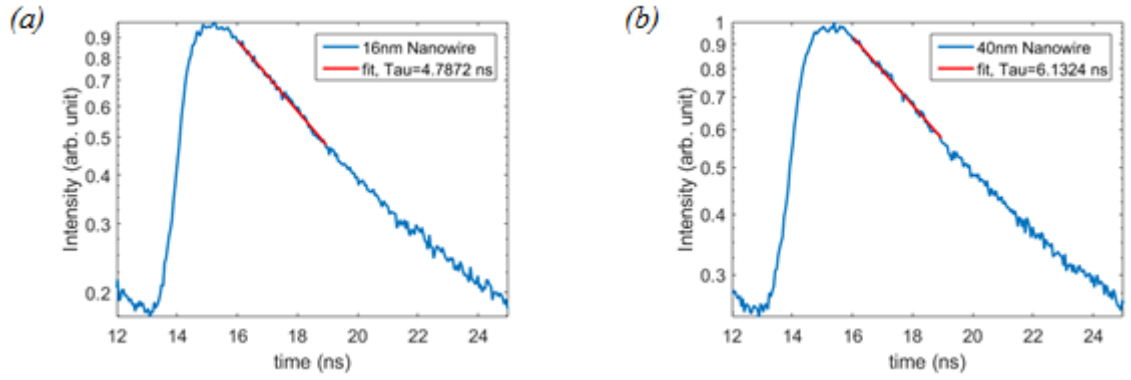

Figure 3-8: The TRPL measurement result from the plain nanowires with the diameter of 16nm (a), and 40nm (b).

For the core-shell nanowires, the result of the TRPL was expected to have a longer lifetime compared to the plain nanowire. As discussed in 3.1.2, it is not clear to specify the peak of the core nanowire with 16nm, and 20nm nanowire. Therefore, only the 40nm core-shell nanowire was measured with the variation of Ga compositions in the shell. The result of the TRPL for three wires with different shell compositions is shown in Figure 3-9 (a). For each shell composition, a number of nanowires were measured. The average lifetime is presented in Figure 3-9 (b) and the error bars represent the standard deviation for the measured wires. The lifetime of the core-shell nanowire increased with an increasing of Ga compositions, i.e. an increasing shell bandgap.

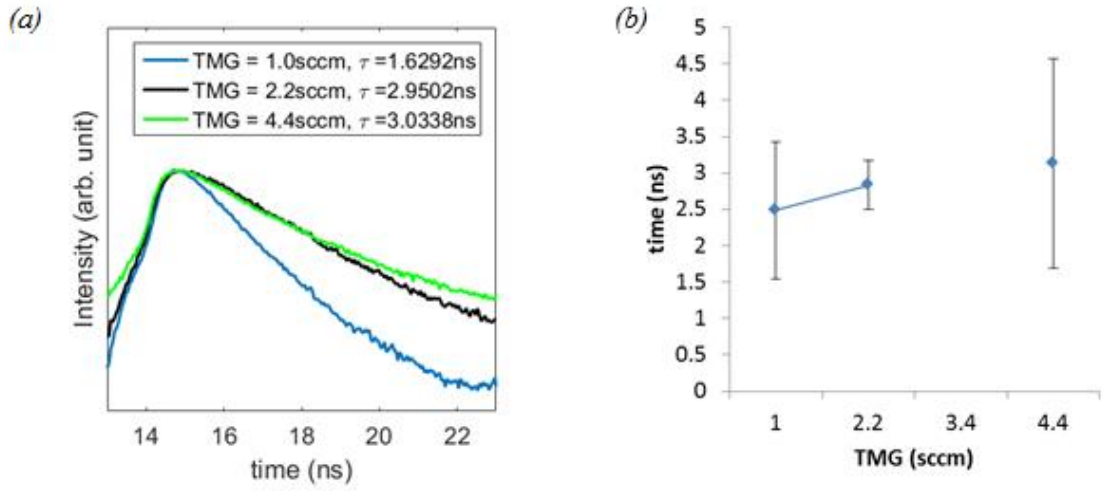

Figure 3-9: (a) The TRPL of the core-shell nanowire at the different Ga compositions of the shell according to the variation of TMG flow. (b) The plot between the TMG flow and the average lifetime.

With a larger bandgap in the shell layer, more carriers tend to move to the lower bandgap material of the core nanowire. Therefore, the lifetime of the surface passivated nanowire can be improved as the band offset is increased. However, an increasing of Ga compositions could possibly introduce more dislocation defects related to the lattice mismatch as mentioned in 3.1.2. There would be a maximum lifetime before it is shortened by the non-radiative recombination process through the dislocation defects.

It is expected that the lifetime of the core-shell nanowire to be longer than the plain nanowire, because the shorter lifetime indicates the influence of the non-radiative recombination. In contrast with that expectation, the result of the measurements shows that the lifetime of the core-shell nanowire is actually shorter than the plain nanowire as shown in Table 3-1. One possible reason for this effect could be that the core-shell nanowires were grown in a separate growth series a couple of months after the plain nanowires. With the different growth series, the actual material composition of the wires might be varied. This could increase another non-radiative recombination center which were not surface related

	Diameter (nm)	Average lifetime (ns)	SD (ns)
Plain nanowire	16	4.80	0.99
	40	6.16	1.80
Core-shell nanowire	40	3.13	1.44

Table 3-1: The summarized of the average lifetime and its standard deviation (SD) from plain nanowire and core-shell nanowire

3.3. Temperature Dependent Photoluminescence (TDPL)

For the TDPL studies which aims at finding the activation energy for non-radiative recombination and to compare the quantum efficiencies at low and high temperature, PL spectra were measured on plain InGaP nanowire with the diameters of 40 nm. There was only a single measurement performed on a particular nanowire, so there is no statistical data for these measurements. The studies were made at various temperatures starting from the lowest

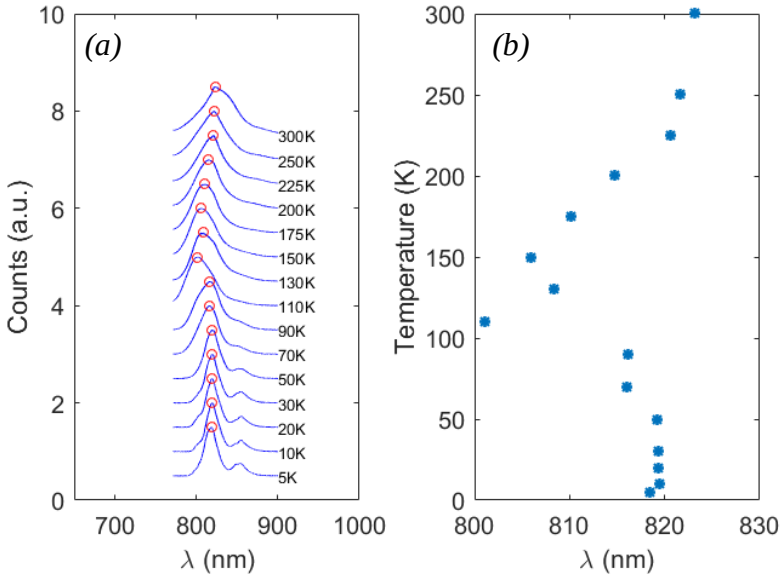

Figure 3-10: (a) The PL spectrum of the 40nm nanowire at the different temperatures. The intensities were normalized, and the actual intensities decreased with increasing temperature as shown in Fig. 3-11. (b) The change of the peak position vs. the temperature from a particular nanowire.

temperature of 5 K to the room temperature (300 K). The PL spectrum of the nanowire is red-shifted at the temperature below 50 K. Then, it turns to be blue-shifted until the temperature is above 150 K which it becomes red-shifted again, Figure 3-10.

The observed spectrum shift is in contrast with the shift of a bulk semiconductor for which its relation between the band gap energy and the temperature are governed by Varshni empirical equation [15];

$$E_g = E_0 - \alpha T^2/(T+\beta) \qquad \text{eq. 12}$$

where E_0 is the transition energy at 0K, and α and β are Varshni thermal coefficients. According to eq. 12, the PL spectrum of a bulk semiconductor should red-shift with increasing temperature and the initial blue-shift observed in Figure 3-10 (b) is therefore unexpected. The same phenomena as Figure 3-10 can also be found in InGaN/GaN multi-quantum wells (MQWs) referring to *Cho et al.*[16] and *Teo et al.*[17]. As explained by *Cho et al.*[16], this interchanging of the shifting direction is an effect of carrier localization within fluctuation potentials of an alloy material. The localization affects the recombination process at low temperature which causes the blue-shift.

Not only is the shifted spectrum observed as the temperature changes, but there was also a quenching of PL intensity. Figure 3-11 (a) illustrates the quenching on an Arrhenius plot which is a normalized integrated PL intensity plot against the inverse temperature. The quenching started at the temperature higher than 50 K. From the plot, the intensity is almost two orders of magnitude lower at room temperature.

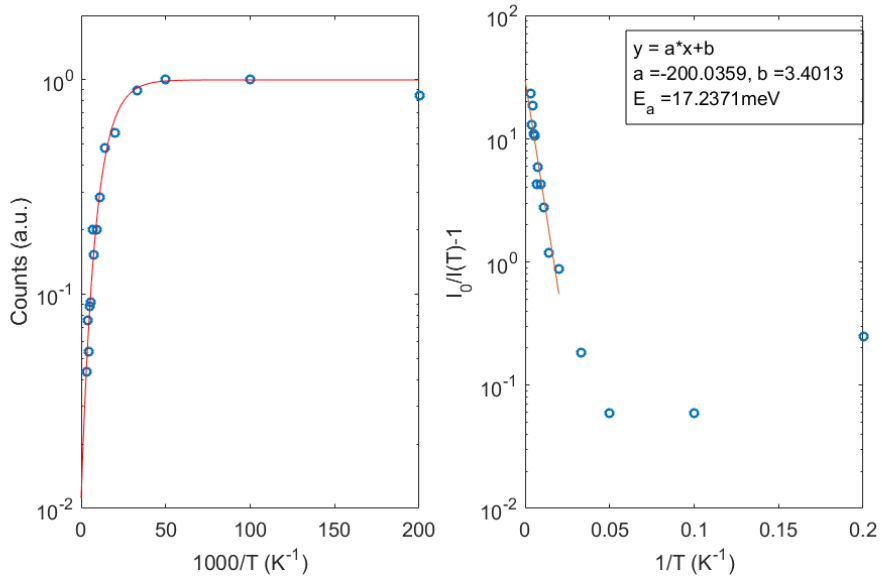

Figure 3-11: (a) The plot is Arrhenius plot showing the variation of integrated PL intensity as a function of temperature. (b) The plot is the modification of Arrhenius plot to achieve $\boldsymbol{E_a}$.

The relation between the temperature and the integrated PL intensity is expressed as eq. 13 [18]. A constant I_0 is intensity at 0K and k is a Boltzmann's constant. Parameters α and E_a are process rate parameter and activation energy, respectively.

$$I(T) = \frac{I_0}{1 + \alpha \exp(-{}^{E_a}/_{kT})} \qquad \text{eq. 13}$$

$$\ln(I_0/I(T) - 1) = \ln(\alpha) - {}^{E_a}/_{kT} \qquad \text{eq. 14}$$

By modifying eq. 13 into a linear equation as eq. 14, the activation energy can be achieved from the slope of the plot divided by Boltzmann's constant, Figure 3-11 (b).

The fit in Figure 3-11 (b) disregards the data below 50 K where the intensity has the temperature dependence weaker than the measurement accuracy. Furthermore, the activation energy could not be evaluated explicitly at low temperature due to too few data points and lacking of statistical data. The activation energy at low temperature, E_a, is expected to be a couple of meV as observed by *Titova et al.*[19] which performed a similar measurement on GaAs-AlGaAs core-shell nanowire. The high temperature activation energy, E_a^*, was measured to be 17.2 meV (red line fit in Figure 3-11 (b)). The value of E_a^* is roughly the same as measured by *Titova et al.*[19].

The activation energy at low temperature is expected to originate from an ionization of excitons [19]. At high temperature, the activation energy is expected to originate from the temperature dependence of the capture cross section of non-radiative recombination centers as explained by *Krustok* [18]. Due to an increasing of carriers' thermal energy as the temperature

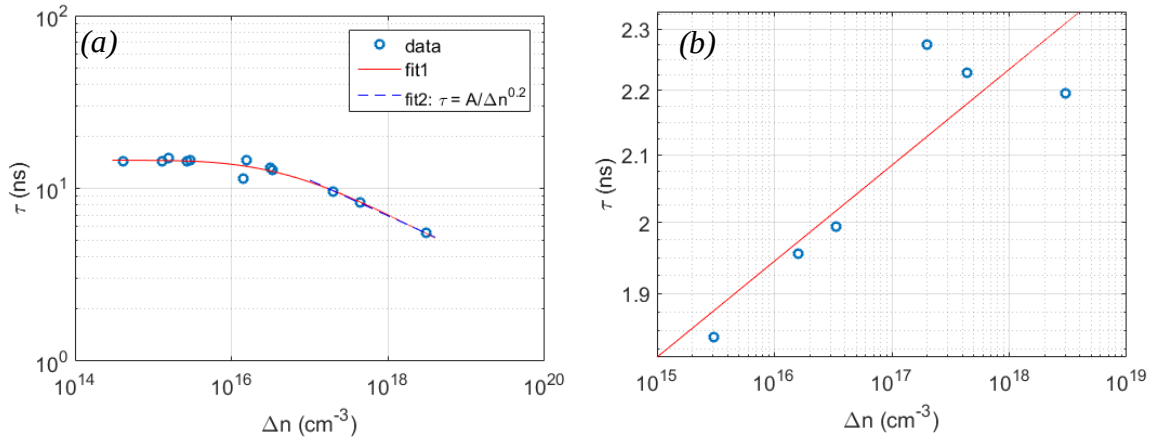

Figure 3-12: Carrier lifetime (tau) vs. injected concentration Δn at (a) 5 K, and (b) 100 K.

increases, the carriers can therefore reach the non-radiative recombination centers at high temperature.

Since the quenching has two different rates between the low temperature and the high temperature, further studies to understand the different decay processes were evaluated by the power dependent TRPL measurement at two different temperatures. The variation of the laser power provides a different carrier injection concentration, Δn. As a result, the plot of Δn vs the total lifetime of the nanowire at 5 K and 100 K is shown in Figure 3-12. One should expect to get the power dependent lifetime plot as shown in Figure 1-3.

For the low temperature case, Figure 3-12 (a), the total lifetime looks the same as the radiative lifetime or the Auger lifetime in Figure 1-3. The plot in this case is constant at the LLI and starts to decrease at the injection level higher than the equilibrium concentration, n_0, of the nanowire (~10^{16} cm^{-3}). Therefore, the total lifetime in this case is not limited by the SRH recombination lifetime according to Figure 1-3. As aforementioned, the capture cross section of the defect is temperature dependence which has not been activated at the low temperature. To find the limiting recombination process at low temperature, an equation, $\tau = A/\Delta n^x$, is used for the fitting line of the last three data points in the plot, Figure 3-12 (a). The equation is an estimated lifetime at the HLI for both radiative ($x = 1$, eq. 5) and Auger ($x = 2$, eq. 8) recombination. The value of x from the plot is about 0.2 which is not close to either radiative or Auger recombination process. Therefore, it is possible that the measurement was just on the turning point between the LLI and the HLI. It could not be identified which recombination is the limiting process.

For the high temperature case, Figure 3-12: (b), the total lifetime increases with increasing injection concentration, which indicates that the recombination process is dominated by SRH recombination (Figure 1-3). That means the carrier's capture cross section is activated at high temperature with the activate energy, E_a^*.

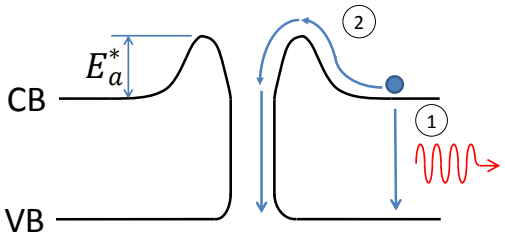

Figure 3-13: The schematic of activation energy for the carrier's capture cross section. The recombination process (1) is the radiative recombination and (2) is the SRH recombination.

Figure 3-13 is a schematic illustrating two different recombination paths regarding the activation energy of non-radiative recombination center [20]. At low temperature, the carriers would recombine through the radiative recombination process, path 1. When the carriers get a sufficient thermal energy at increasing temperature, they could overcome the activation energy and recombine through path 2 which is the non-radiative recombination process. The vertical line connecting CB and VB represents the distribution of energy state along the bandgap for the surface SRH. As a result, the SRH recombination could compete with the other recombination mechanisms at high temperature. Consequently, the lifetime at the high temperature is shorter than at the lower temperature.

4. Conclusions and outlooks

The TRPL measurement of the plain nanowire with different diameters gives a shorter lifetime for the 16 nm nanowire compared to the 40 nm nanowire. This result is expected since the thinner wire has a larger surface-to-volume ratio. By comparing the lifetime of the plain nanowire (6.13 ns) to InP reference sample (13.7 ns), the IQE would be about 50% lower for the nanowire. However, the main uncertainty of this reference is the radiative lifetime which depends on the doping concentration. Ideally, the bulk reference sample would need to have the same doping level as the wires and a very high crystal quality, so that there are no non-radiative recombination centers.

For the core-shell nanowire, the non-radiative recombination via the surface SRH mechanism should have less effect on the lifetime. As a result, the lifetime of the core-shell nanowire is expected to last longer than the plain nanowire. A trend could be seen within the series of wires with different shell composition; the larger the bandgap of the shell, the longer the lifetime of the nanowire. This is an indication of a surface passivating effect. Nonetheless, the lifetime might be shortened with further increasing shell bandgap, due to the strain effects inducing a non-radiative recombination centers between the core and the shell.

Unfortunately, the lifetimes of all the core-shell nanowires are lower than the plain nanowire. Due to the different growth series of the plain and the core-shell nanowire, the actual material composition of the sample might not be compatible. For future studies, all samples should be grown in the same growth series to minimize the effects of variations in the unintentional doping level and the density of non-radiative recombination centers which are not surface related. Thus, it might also include material characterization measurements to ensure the correlation between each growth. Another explanation is that the strain between the core nanowire and the shell layer leads to the formation of dislocation defects, which are centers for non-radiative recombination. It could also be that the shell actually introduces some non-radiative defects which degrades the IQE.

First observation of TDPL measurement on plain nanowire is the blue-shifted effect at low temperature which is expected to be the red-shifted effect for bulk semiconductor. Another observation on the TDPL results of the plain nanowire is a quenching of the luminescence at high temperature due to the excess thermal energy of the carriers which overcome the activation energy and, as a result, leave the confined potential. Moreover, the Arrhenius plot shows that the internal quantum efficiency is two orders of magnitude higher at low temperature (5K) compared with room temperature (300K). The fit of the Arrhenius plot, Figure 3-11 (b), indicates two different slopes corresponding to two activation energies at the temperatures below and above 50K.

For the power dependent TRPL at low temperature (5K), the measurement on the plain nanowire at higher excitation power may need to be performed to identify the exact limiting process. The same study at high temperature (100K) shows a result with much shorter lifetime than the low temperature study. The lifetime in this case is increased as the function of the

injection carrier concentration. This means the lifetime is dominated by the SRH recombination. The non-radiative recombination mechanism does not become critical until the temperature is above 50K as shown in Arrhenius plot. At that point, the carriers achieve a sufficient thermal energy to overcome the activation energy of the non-radiative recombination center (E_a^* =17.2meV). Future studies should also include the same measurement on the core-shell nanowires at low and high temperature.

5. Self-reflection

My thesis work aims to study the IQE of a ternary alloy nanowire. There were three experiments performed in the study, which are Photoluminescence (PL) spectroscopy, Time-resolved Photoluminescence (TRPL), and Temperature Dependent Photoluminescence (TDPL). All these experiment was used to understand the non-radiative recombination center. Whereupon, the IQE of the nanowire was expected to be improved as a result.

By setting up equipment for the experiments, I acquired a lot of hands-on experiences in an optical alignment, especially a fiber coupling. Furthermore, I got an idea that there is no such a perfect method for each measurement. The one that can give an optimized result should be selected for the studies. For example; Instead of the streak camera, which is generally used for the TRPL measurement, an Avalanche photodiode (APD) was used. Even the equipment has the lower temporal resolution, the higher quantum efficiency of the equipment is more preferable for the TRPL measurement on InGaP nanowire.

The technique called Time-correlated Single Photon Counting (TCSPC) was applied with the APD for the time-resolved measurement. The technique which was new for me is a robust time-dependent method used to capture a single photon event.

From the measurement results, it required literature review and discussions with the supervisor to analyze and understand the data from the experiment. Even there are limitations of the measurement which gives only a few data point for analysis; it still gave enough information to compare with the reference research paper. As a result, they provided more understanding about the non-radiative recombination center at different excitation power and temperature.

The studies were the very first TRPL measurement on the ternary alloy nanowire at Solid State Division, Lund University. Also, the experiment setup could be able to collect the luminescence with five orders of magnitude different in the excitation power. Moreover, the TRPL measurement system set up for this study could also be used for other research in the future; e.g. a single photon emission from the quantum dot.

References

[1] J. Wallentin, N. Anttu, D. Asoli, M. Huffman, I. Åberg, M.H. Magnusson, G. Siefer, P. Fuss-Kailuweit, F. Dimroth, B. Witzigmann, Science, 339 (2013) 1057-1060.
[2] C.P.T. Svensson, T. Mårtensson, J. Trägårdh, C. Larsson, M. Rask, D. Hessman, L. Samuelson, J. Ohlsson, Nanotechnology, 19 (2008) 305201.
[3] X. Duan, Y. Huang, R. Agarwal, C.M. Lieber, Nature, 421 (2003) 241-245.
[4] S. Rein, Lifetime spectroscopy: a method of defect characterization in silicon for photovoltaic applications, Springer Science & Business Media2006.
[5] D.K. Schroder, Semiconductor material and device characterization, John Wiley & Sons2006.
[6] B.E.A. Saleh, M.C. Teich, Wiley, Somerset, 2013.
[7] C.-C. Chang, C.-Y. Chi, M. Yao, N. Huang, C.-C. Chen, J. Theiss, A.W. Bushmaker, S. LaLumondiere, T.-W. Yeh, M.L. Povinelli, C. Zhou, P.D. Dapkus, S.B. Cronin, Nano Letters, 12 (2012) 4484-4489.
[8] W. Becker, Advanced Time-Correlated Single Photon Counting Applications, Springer International Publishing2015.
[9] A. Patane, N. Balkan, Semiconductor Research: Experimental Techniques, Springer Berlin Heidelberg2012.
[10] G.H. Olsen, T.Z. Zamerowski, R.T. Smith, E.P. Bertin, Journal of Electronic Materials, 9 977-987.
[11] A. Mishra, L. Titova, T. Hoang, H. Jackson, L. Smith, J. Yarrison-Rice, Y. Kim, H. Joyce, Q. Gao, H. Tan, Applied Physics Letters, 91 (2007) 263104.
[12] H. Brune, K. Kern, Growth and Properties of Ultrathin Epitaxial Layers, 8 (1997) 149.
[13] J. Trägårdh, Optical spectroscopy of single nanowires, Lund University2008.
[14] K. Pemasiri, M. Montazeri, R. Gass, L.M. Smith, H.E. Jackson, J. Yarrison-Rice, S. Paiman, Q. Gao, H.H. Tan, C. Jagadish, Nano letters, 9 (2009) 648-654.
[15] Y.P. Varshni, Physica, 34 (1967) 149-154.
[16] Y.-H. Cho, G.H. Gainer, A.J. Fischer, J.J. Song, S. Keller, U.K. Mishra, S.P. DenBaars, Applied Physics Letters, 73 (1998) 1370-1372.
[17] K.L. Teo, J.S. Colton, P.Y. Yu, E.R. Weber, M.F. Li, W. Liu, K. Uchida, H. Tokunaga, N. Akutsu, K. Matsumoto, Applied Physics Letters, 73 (1998) 1697-1699.
[18] J. Krustok, H. Collan, K. Hjelt, Journal of Applied Physics, 81 (1997) 1442-1445.
[19] L. Titova, T.B. Hoang, H. Jackson, L. Smith, J. Yarrison-Rice, Y. Kim, H. Joyce, H. Tan, C. Jagadish, (2006).
[20] J.I. Pankove, Optical processes in semiconductors, Courier Corporation2012.